

Peristaltic pumping of a viscoelastic fluid at high occlusion ratios and large Weissenberg numbers

Hector D. Ceniceros

Department of Mathematics, University of California Santa Barbara, CA 93106

Jordan E. Fisher

Department of Mathematics, University of California Santa Barbara, CA 93106

Abstract

Peristaltic pumping is a mechanism for transporting fluid or immersed particles in a channel by waves of contraction. It occurs in many biological organisms as well as in several human designed systems. In this study, we investigate numerically the peristaltic pumping of an incompressible viscoelastic fluid using the simple Oldroyd-B model coupled to the Navier-Stokes equations. The pump's walls are assumed to be massless immersed fibers whose prescribed periodic motion and flow interaction is handled with the Immersed Boundary Method. We utilize a new, highly efficient non-stiff version of this method which allows us to explore an unprecedented range of parameter regimes, nearly all possible occlusion ratios and Weissenberg numbers in excess of 100. Our numerical investigation reveals rich, highly concentrated stress structures and new, striking dynamics. The investigation also points to the limitations of the Oldroyd B model, with a potential finite time blow-up, and to the role of numerical regularization.

Keywords: Oldroyd-B, peristaltic, Immersed Boundary, semi-implicit method

Email addresses: hdc@math.ucsb.edu (Hector D. Ceniceros), www.math.ucsb.edu/~hdc (Hector D. Ceniceros), jordan@math.ucsb.edu (Jordan E. Fisher)

1. Introduction

Peristalsis is the flow that takes place in a channel with flexible walls due to a series of contraction or expansion waves along the walls. It is a predominant mechanism of action in a variety of biological phenomena, from earthworm mobility [25] to gastrointestinal [14] and esophageal transport [2]. Peristalsis is utilized in many mechanical fluid pumps, often because of its ability to effectively transport highly viscous fluids and as well as immersed particles. In both biological and mechanical systems, the fluid internal to the pump may be non-Newtonian. Such is the case for peristalsis in the oviduct [5] and uterus [18] where the transported biological fluid is highly viscoelastic [17].

There are several analytical and numerical studies of peristalsis [27, 16, 15, 6, 24, 29, 13, 32, 11, 10, 36] with increasing emphasis on viscoelastic fluids. We focus here on a model used by the recent investigations of Teran, Fauci, and Shelley [32] and by Chrispell and Fauci [10]. The fluid model is based on the Stokes [32] or Navier-Stokes [10] equations coupled with the simple Oldroyd-B (OB) model and describes a dilute solution of flexible polymeric molecules represented by Hookean dumbbells [4, 12, 19]. The Immersed Boundary (IB) Method [21, 22] is employed to model the pump, as done originally by Fauci [13]. In this IB setting, the pump's walls are tethered to anchor points which are set to a prescribed periodic motion to simulate the waves of contraction and expansion. Teran, Fauci, and Shelley [32] and Chrispell and Fauci [10] found that there is a marked difference between the Newtonian and the non-Newtonian fluid pumping. In particular, the mean flow rate is noticeably affected by viscoelastic effects. They also noted that extremely strong normal stresses are generated at the pump's constriction as the amplitude of the peristaltic wave relative to the channel width (the so called occlusion ratio) increases, even for moderate Weissenberg numbers (the polymer relaxation time relative to the flow's characteristic time scale). These large normal stresses present a formidable computational challenge; to accurately preserve the structure of the pump's walls during their prescribed periodic motion very stiff boundary forces must be employed. This induces a severe time step restriction for explicit IB methods [31, 30]. Indeed, the use of an explicit IB method in [32, 10] limited the parameter space amenable to simulation to a region consisting of only the first half of the possible occlusion ratios and to Weissenberg numbers less or equal to 5. In this work, we employ a novel semi-implicit IB method [8, 7] to make possible a computa-

tional study that covers nearly all possible occlusion ratios and Weissenberg numbers in excess of 100. Our numerical investigation reveals new, striking dynamics which include highly localized stress structures, a potential finite time blow-up, symmetry breaking transitions, and the emergence of a critical occlusion ratio at which the ordering of the mean flow rate with respect to the Weissenberg number is reversed.

The rest of this article is organized as follows. First, the model is described in detail in the following section. Then, in Section 3, we present a new numerical method coupling a viscoelastic fluid solver to a novel, highly efficient semi-implicit version of the IB method, [8, 7]. Our numerical results are presented and discussed in Section 4. Finally, some concluding remarks are given in Section 5.

2. The Peristaltic Pump and Viscoelastic Fluid Models

We consider a peristaltic pump immersed in a periodic 2D domain $\Omega = [0, 1] \times [0, 1]$. We model the peristaltic pump's walls as two disconnected sinusoidal curves [13, 32, 10]

$$\mathbf{X}(t) = \left\{ \left(\xi, \frac{1}{2} + d(\xi, t) \right) \mid \xi \in [0, 1] \right\} \cup \left\{ \left(\xi, \frac{1}{2} - d(\xi, t) \right) \mid \xi \in [0, 1] \right\}, \quad (1)$$

where

$$d(x, t) = \frac{\alpha}{2\pi} [1 + \chi \sin 2\pi(\xi - t)]. \quad (2)$$

Both the spatial and temporal period of the pump is fixed at 1. As time progresses, the waves of peristalsis move from left to right, forcing the fluid to flow to the right (in aggregate). The parameter χ represents the occlusion ratio of the pump. The value $\chi = 0$ corresponds to a straight channel, with no waves of peristalsis, while $\chi = 1$ correspond to a completely occluded channel with the peaks of each sinusoidal curve meeting at some point along the horizontal line $y = 1/2$. The parameter α controls the aspect ratio of the channel. For this work we fix $\alpha = 1.5$.

We model the interior and exterior of the valve as a dilute, incompressible OB suspension [4]. The interaction between the valve and the fluid is

captured via the IB Method. The continuous equations are then

$$Re \left(\frac{\partial \mathbf{u}}{\partial t} + \mathbf{u} \cdot \nabla \mathbf{u} \right) = -\nabla p + \nabla^2 \mathbf{u} + \beta \nabla \cdot \mathbf{S} + \mathbf{f}, \quad (3)$$

$$\nabla \cdot \mathbf{u} = 0, \quad (4)$$

$$\frac{\partial \mathbf{X}}{\partial t} = \mathbf{u}(\mathbf{X}, t), \quad (5)$$

$$\mathbf{S}^\nabla = -We^{-1}(\mathbf{S} - \mathbf{I}). \quad (6)$$

Here \mathbf{f} is a very stiff force acting on the immersed walls binding the current configuration \mathbf{X} to the desired prescribed position given by (1). In (3), Re is the Reynolds number which is a measure of the viscous dissipation relative to inertial forces. The dimensionless term β specifies the strength of the viscoelastic force $\nabla \cdot \mathbf{S}$. Here, \mathbf{S} is the deviatoric part of the viscoelastic stress tensor and evolves according to the OB constitutive equation, given in (6) [4]. \mathbf{S}^∇ denotes the upper convected derivative of \mathbf{S} :

$$\mathbf{S}^\nabla = \frac{d\mathbf{S}}{dt} + \mathbf{u} \cdot \nabla \mathbf{S} - \nabla \mathbf{u} \cdot \mathbf{S} - \mathbf{S} \cdot \nabla \mathbf{u}^T. \quad (7)$$

We is the Weissenberg number and is defined as the ratio of the polymer relaxation time and a characteristic time scale of the fluid. In the limit as $We \rightarrow 0$ the polymeric stress is fixed as the identity tensor \mathbf{I} and the fluid becomes Newtonian.

Finally, the product βWe can be interpreted as the ratio of the polymeric viscosity to the solvent viscosity [32]. We fix $\beta We = \frac{1}{2}$ following [32]. We choose the characteristic length scale to be 1, the width of our fluid domain Ω and the characteristic time scale we also take it to be 1, the period of the peristaltic pump. We fix the Reynolds number of our fluid at $Re = 1$. Throughout this work the only *fluid* parameter we change is the Weissenberg number We .

We discretize the pump's walls \mathbf{X} as a collection of N_B immersed points $\{\mathbf{X}_j\}$. The position of these points is not directly prescribed, rather we construct an artificial force to approximately constrain the immersed points to their respective positions. For each point \mathbf{X}_j , we define \mathbf{T}_j to be the desired target position. We then induce a force \mathbf{F} on immersed points given by

$$\mathbf{F} = \sigma(\mathbf{T} - \mathbf{X}). \quad (8)$$

The stiffness coefficient σ is a numerical parameter. In the limit as $\sigma \rightarrow \infty$ we exactly constrain \mathbf{X} to the desired configuration. In practice, σ needs to be a fairly large value. With our semi-implicit method we can use values of σ multiple orders of magnitude larger than previously possible. For the large values of χ and We explored in this work, we are required to take $\sigma = O(10^6)$ to maintain the structure of the pump. This large stiffness coefficient would lead to prohibitively small time-steps for explicit methods. In our numerical experiments our choice of σ reduces deviations in \mathbf{X} from the target position \mathbf{T} to less than 0.0005 units, even when the normal polymeric stresses at the pump's walls rise to values of 1000 and more.

3. Numerical Methodology

We briefly overview the numerical method here. It is based on a semi-implicit discretization of the Navier-Stokes equations given by

$$\frac{\mathbf{u}^{n+1} - \mathbf{u}^n}{\Delta t} + \mathbf{u}^n \cdot \nabla \mathbf{u}^n = -\mathbf{D}_h p^{n+1} + L_h \mathbf{u}^{n+1} + \mathbf{f}, \quad (9)$$

$$\mathbf{D}_h \cdot \mathbf{u}^{n+1} = 0, \quad (10)$$

$$\frac{\mathbf{X}^{n+1} - \mathbf{X}^n}{\Delta t} = \mathcal{S}_n^* \mathbf{u}^{n+1}. \quad (11)$$

Here a superscript n denotes a numerical approximation taken at the time $n\Delta t$ and Δt is the timestep. The spatial operators \mathbf{D}_h and L_h are the standard, second order approximations to the gradient and the Laplacian, respectively. The convection term $\mathbf{u}^n \cdot \nabla \mathbf{u}^n$ is handled separately via a third-order essentially non-oscillatory (ENO) scheme [28]. The force \mathbf{F} in (8) is defined at the immersed boundary only and has to be spread onto the surrounding Eulerian grid points. Likewise, the velocity field is not given at the immersed boundary, so we must *interpolate*. To achieve this spreading and interpolation we define the adjoint operators:

$$(\mathcal{S}_n G)(\mathbf{x}) = \sum_{s \in \mathcal{G}_B} G(s) \delta_h(\mathbf{x} - \mathbf{X}^n(s)) h_B, \quad (12)$$

$$(\mathcal{S}_n^* w)(s) = \sum_{\mathbf{x} \in \mathcal{G}_\Omega} w(\mathbf{x}) \delta_h(\mathbf{x} - \mathbf{X}^n(s)) h^2, \quad (13)$$

known as the spreading and interpolation operators, respectively. Here $\delta_h(\mathbf{x}) \equiv d_h(x)d_h(y)$ is an approximation to the two-dimensional Dirac delta distribu-

tion and d_h is given by

$$d_h(r) = \begin{cases} \frac{1}{4h} (1 + \cos(\frac{\pi r}{2h})) & \text{if } |r| \leq 2h, \\ 0 & \text{otherwise.} \end{cases} \quad (14)$$

We refer to these operators as lagged because the interface configuration \mathbf{X}^n is used instead of the future configuration \mathbf{X}^{n+1} .

Utilizing \mathcal{S}_n and \mathcal{S}_n^* we now specify the form of \mathbf{f} in (9):

$$\mathbf{f} = \sigma \mathcal{S}_n(\mathbf{T}^{n+1} - \mathbf{X}^{n+1}) + \beta \mathbf{D}_h \cdot \mathbf{S}^n, \quad (15)$$

which incorporates both the artificial force on the immersed points, as well as the additional force coming from the polymeric stress. We thus consider the polymeric stress fixed as we update the fluid. Once we have an updated fluid velocity \mathbf{U}^{n+1} we will then calculate an updated value for the stress \mathbf{S}^{n+1} .

We can eliminate \mathbf{u}^{n+1} from the equations (9)-(11) to arrive at a *linear* system of the form [8, 7]

$$\mathbf{X}^{n+1} = \sigma \mathcal{M}_n(\mathbf{T}^{n+1} - \mathbf{X}^{n+1}) + \mathbf{b}^n, \quad (16)$$

We refer to this as the Lagrangian system. \mathcal{M}_n is a linear operator acting on a force distribution \mathbf{F} and returning the resulting displacement of immersed points due to the induced fluid flow from the spread force $\mathcal{S}_n \mathbf{F}$. One important observation is that both \mathcal{M}_n and \mathbf{b}^n can be explicitly constructed in an efficient manner, yielding a $2N_B \times 2N_B$ matrix and $2N_B$ vector respectively. This construction is detailed in [8]. The resulting system can be rewritten as a simple matrix inversion problem

$$(I + \sigma \mathcal{M}_n) \mathbf{X}^{n+1} = \sigma \mathbf{T}^{n+1} + \mathbf{b}^n, \quad (17)$$

The matrix $I + \sigma \mathcal{M}_n$ is positive-definite and the linear system (17) can be efficiently solved. Here we employ the conjugate gradient to obtain a nearly optimal solver. Once we have solved (17) for the updated configuration \mathbf{X}^{n+1} we then calculate the updated fluid velocity via (9)-(10).

Finally, we must calculate the updated polymeric stress \mathbf{S}^{n+1} . We use the method of lines and consider the semi-discrete equation:

$$\frac{d\mathbf{S}}{dt} + \mathbf{u}^{n+1} \cdot \nabla \mathbf{S} = \mathbf{D}_h \mathbf{u}^{n+1} \cdot \mathbf{S} + \mathbf{S} \cdot \mathbf{D}_h (\mathbf{u}^{n+1})^T + \frac{1}{We} (\mathbf{I} - \mathbf{S}). \quad (18)$$

Here the convective term $\mathbf{u}^{n+1} \cdot \nabla \mathbf{S}$ is calculated via the third-order ENO scheme, as is the convection in the momentum equation (9). We further discretize in time via a second-order Runge-Kutta (RK) method [28]. If we define the Euler update operator

$$E(\mathbf{S}) = \mathbf{S} + \Delta t \left[\mathbf{D}_h \mathbf{u}^{n+1} \cdot \mathbf{S} + \mathbf{S} \cdot \mathbf{D}_h (\mathbf{u}^{n+1})^T + \frac{1}{We} (\mathbf{I} - \mathbf{S}) - \mathbf{u}^{n+1} \cdot \nabla \mathbf{S} \right], \quad (19)$$

then the RK update is given as $\mathbf{S}^{n+1} = (\mathbf{S}^n + E(E(\mathbf{S}^n)))/2$. It is important to note that if $E(\cdot)$ is total variation diminishing (TVD) then so is the RK method [28].

3.1. Summary of algorithm

Given \mathbf{X}^n , \mathbf{u}^n , \mathbf{S}^n at time $t = n\Delta t$, a complete timestep may be summarized as follows

1. Calculate the fluid matrix \mathcal{M}_n and the explicit term \mathbf{b}^n .
2. Solve for the updated pump configuration \mathbf{X}^{n+1} via the matrix problem $(I + \sigma \mathcal{M}_n) \mathbf{X}^{n+1} = \sigma \mathbf{T}^{n+1} + \mathbf{b}^n$.
3. Calculate the updated fluid velocity \mathbf{u}^{n+1} via (9)-(10).
4. Calculate the updated polymeric stress \mathbf{S}^{n+1} via the second-order (TVD) RK method, $\mathbf{S}^{n+1} = (\mathbf{S}^n + E(E(\mathbf{S}^n)))/2$.

4. Results

We summarize in this section the results of our numerical simulations. We first provide evidence to validate the numerical methodology and then proceed to examine the dynamics of the peristaltic pump model for occlusion ratios and Weissenberg numbers.

A quantity of interest in the fluid transport is the total mass flux (flow rate) across a specified vertical line $x = x_0$,

$$Q(x_0, t) = \int_{0.5-d(x_0,t)}^{0.5+d(x_0,t)} u(x_0, y) dy. \quad (20)$$

More importantly is the *mean flow rate*, the average mass flux over one time-period, given by

$$\Theta(t) = \frac{\pi}{\alpha \chi} \int_t^{t+1} Q(x_0, t') dt'. \quad (21)$$

The constant $\pi/(\alpha\chi)$ has been introduced to produce a *normalized, dimensionless mean flow rate* such that $\Theta(t) \equiv 1$ when $\chi = 1$, regardless of whether the fluid is Newtonian or viscoelastic. In this work, we take $x_0 = 0.5$ and, as mentioned above, we fix $Re = 1$ and $\beta We = 1/2$. Initially, $\mathbf{S} = \mathbf{I}$ in all our simulations.

4.1. Resolution study and comparison to analytical results

We seek to validate our simulations through two approaches: by performing a resolution and convergence study for the full system as well as by comparing to an analytic formula for Θ valid for a Newtonian Stokes flow.

For the resolution and convergence study we consider the particular case $\chi = 0.25$ and $We = 1$. The flow is smooth for this low χ and We [32, 10] and hence one can verify the theoretical order of convergence of the method. To this end, we fix the time-step, $\Delta t = 0.00025$, and run the simulation for a range of N from 256 up to 2048. We consider the $N = 2048$ run as our reference solution (“exact”) and compute the errors of the other simulations in relation to this $N = 2048$ case. The results are displayed in Fig. 1. In Fig. 1(a) we examine the difference in flow rate $\frac{\pi}{\alpha\chi}Q$ at time $t = 1$. We observe less than a 1% relative error for $N \geq 1024$. In Fig. 1(b) we consider the sup (maximum) norm of the difference of the xx -component of the polymeric stress (S_{xx}). In both cases, we observe a slightly better than first order convergence, as expected [20].

Jaffrin [15] provides an asymptotic formula for the mean flow rate Θ valid for a Newtonian Stokes flow ($Re = 0$ and $We = 0$):

$$\Theta_J = \frac{15\chi^2 + 2\alpha^2[4(1 - \chi^2)^{5/2} + (7\chi^2 - 4)(1 - \chi^2)]}{\chi[5(2 + \chi^2) + 6\alpha^2\chi^2(1 - \chi^2)]}. \quad (22)$$

This formula includes curvature corrections to the simpler relation $\Theta = 3\chi^2/(2 + \chi^2)$ of Jaffrin, Shapiro, and Weinberg [27].

In contrast to the Stokes case, the Navier-Stokes fluid has advection and takes a finite amount of time ($t < 1$) to reach a steady state. We take $t = 1$ and calculate Θ for a full range of χ , from 0 up to 0.95. The comparison of our numerical results to Jaffrin’s formula (22) is given in Fig. 2. We see reasonably good agreement. However, for small to moderate occlusion ratios, the Stokes flow results in [32] provide slightly better agreement with the analytic formula. Based on numerical experience, we believe that in addition to the small difference caused by inertia (c.f. [10]), the main deviation

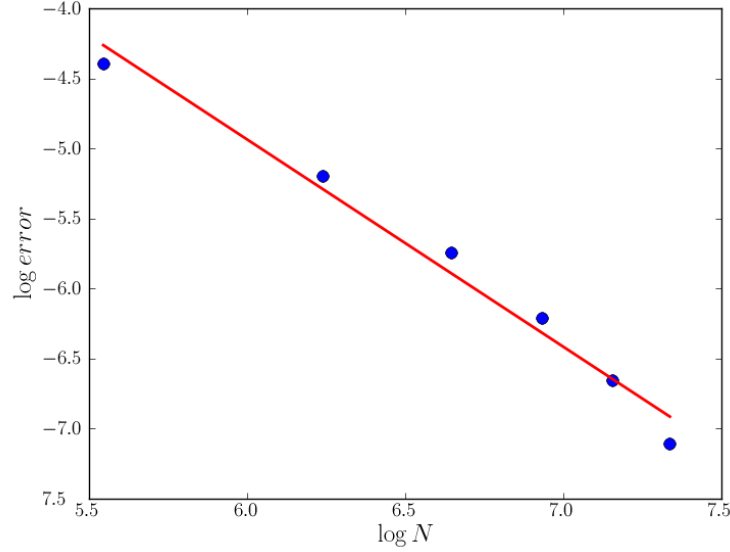
from the analytic result might be attributed to the somewhat better volume conservation of the explicit IB method. Importantly, however, explicit IB simulations for the cases when $\chi \geq 0.5$ are impractical.

4.2. High occlusion ratio, $\chi=0.8$

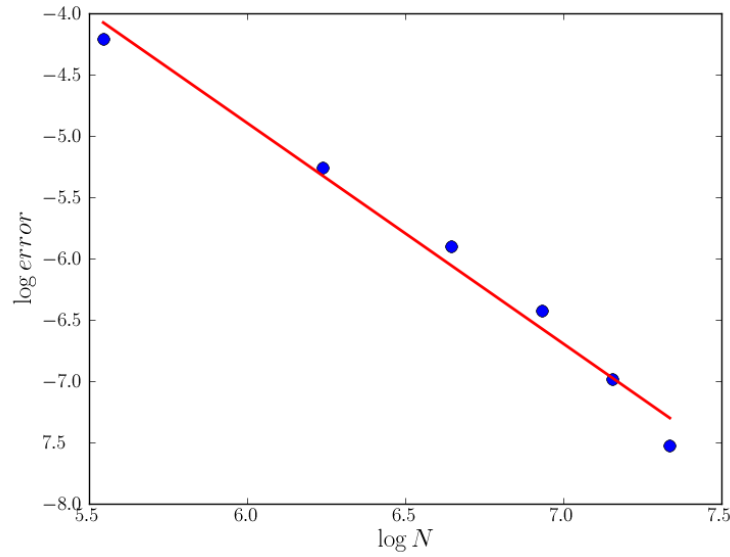
As the occlusion ratio of the peristaltic wave amplitude relative to the channel’s width increases, the fluid generates progressively larger stresses on the peristaltic pump. These stresses become so large that even at mid range occlusion ratios ($\chi \approx 0.5$) and quite moderate Weissenberg numbers ($We \approx 5$) an *explicit*, accurate integration of the IB model ceases to be practical. In more detail, the high values of the stiffness constant σ which are needed to maintain the structure of the pump and to enforce the given periodic motion under high stresses are on the order of 10^6 or higher. These large values become unattainable with an *explicit* integration of the IB equations due to the induced, extremely small time-step constraint, even at modest resolutions ($N \leq 256$) [10]. This has limited previous (explicit) IB simulations of peristaltic pumping of an OB fluid [32, 10] to the restricted region in parameter space consisting of $0 \leq \chi \leq 0.5$ and $0 \leq We \leq 5$. Indeed, the time-step restriction of the explicit IB method becomes so severe that Crispell and Fauci [10] found it necessary to take a much smaller stiffness constant ($\sigma = 2000$) to be able to afford stable simulations for $\chi = 0.5$ and $We = 5$ (no corresponding value of σ was reported in [32]). However, we have found (also [9]) that values of σ much smaller than 10^6 are insufficient to maintain the integrity of the pump for χ near 0.5 or higher and for $We \geq 5$. More precisely, the pump artificially “swells” due to extremely large normal stresses if σ is not large enough and this “swelling” leads to a faux decrease of the mean flow rate. This numerical problem underlies the fact that the accurate computation for even moderate χ and We is a formidable challenge.

With our efficient, implicit IB methodology coupled to the robust scheme for the polymeric stress equation and the use of high order upwinding, we are able to compute reliably for nearly all the occlusion ratio range ($0 \leq \chi < 1$) and for We more than one order of magnitude of what was previously possible. Throughout our computations we closely monitor the constriction of the pump to ensure no artificial swelling is produced for the high occlusion ratios and high Weissenberg numbers we consider.

As an illustration of the rich dynamics exhibited at high occlusion ratios we now present simulation results for $\chi = 0.8$ and $We = 5$. In Figs. 3 through 6, we plot the polymeric stress and the vorticity evolution over time,



(a) Error of flow rate $\frac{\pi}{\alpha\chi}|Q - \tilde{Q}|$, $m = -1.479$.



(b) Error of maximum stress $\|S_{xx} - \tilde{S}_{xx}\|_{\infty}$, $m = -1.800$.

Figure 1: Spatial resolution study for decreasing values of h . Value specified is plotted against h in a log-log plot. Variables with a tilde, $\tilde{\square}$, refer to values coming from an $N = 2048$ simulation. Lines are linear fits with specified slope m .

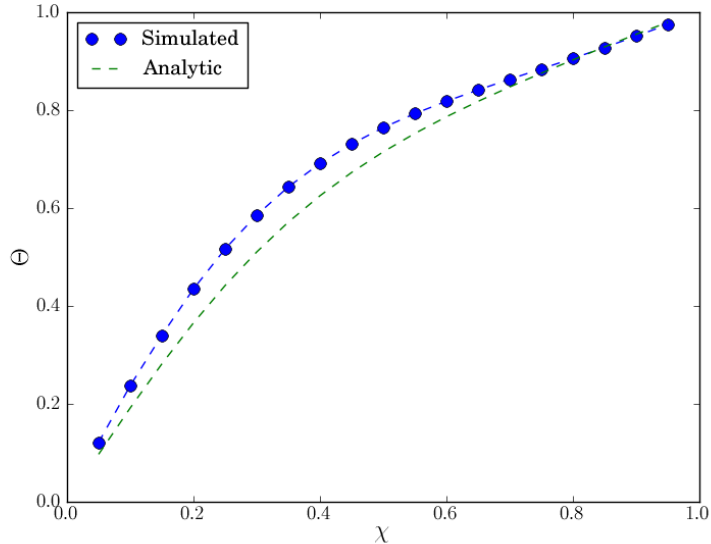


Figure 2: Normalized mean flow calculated both via Jaffrin’s formula and numerical simulation ($Re = 1$) for the full range of $\chi = 0$ to $\chi = 1$.

for $N = 1024$ and $\Delta t = 0.00025$. We see first that S_{xx} , the xx component of the polymeric stress, is largely concentrated in the pump’s constriction (neck), attaining a peak value of 360 at time $t = 0.5$. Near $t = 1.5$, S_{xx} becomes much more localized, into a nearly horizontal line, and grows rapidly reaching a maximum value of 18000. Later ($t = 4.5$), this singly filamented structure splits into two threads running through the pump’s neck. The two additional components of the polymeric stress, S_{xy} and S_{yy} , also develop strong localized structures right after the neck, at the dilated part of the pump, reaching peak values of 2400 and 6400, respectively.

The trace of \mathbf{S} , $\text{tr}(\mathbf{S}) = S_{xx} + S_{yy}$, provides a measure of the mean-squared elongation of the Hookean dumbbells in the OB model. Thus, a look at Fig. 3 and Fig. 5 clearly identifies the filament-like areas where extremely high polymer coil extension takes place. As noted in [32], the stress growth at the pump’s constriction is initially produced by an extensional flow, as the vorticity plot (Fig. 6 at $t = 0.5$) demonstrates. However, at $t = 1.5$ the difference between the vorticity distribution of the Newtonian flow (Fig. 7) and of the viscoelastic counterpart is striking. The localized structures of very high stresses have evolved into two sharp layers adjacent to the inner surface

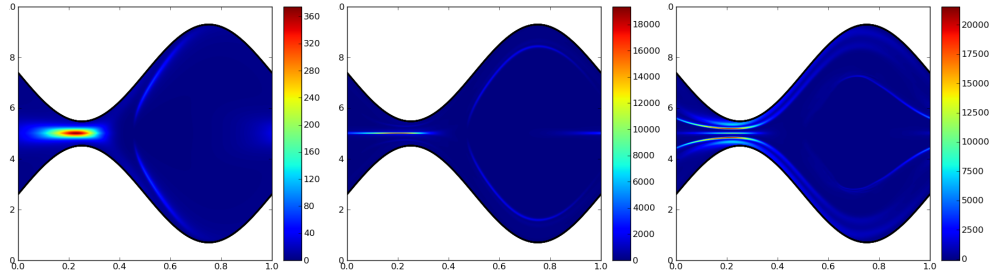


Figure 3: S_{xx} for $We = 5$ and $\chi = 0.8$ at times $t = 0.5, t = 1.5, t = 4.5$.

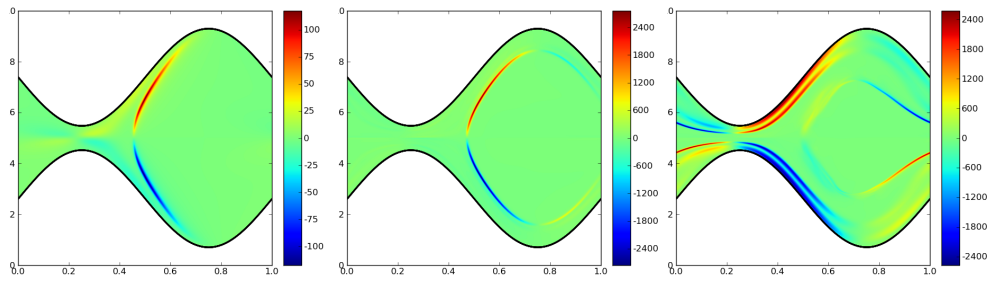


Figure 4: S_{xy} for $We = 5$ and $\chi = 0.8$ at times $t = 0.5, t = 1.5, t = 4.5$.

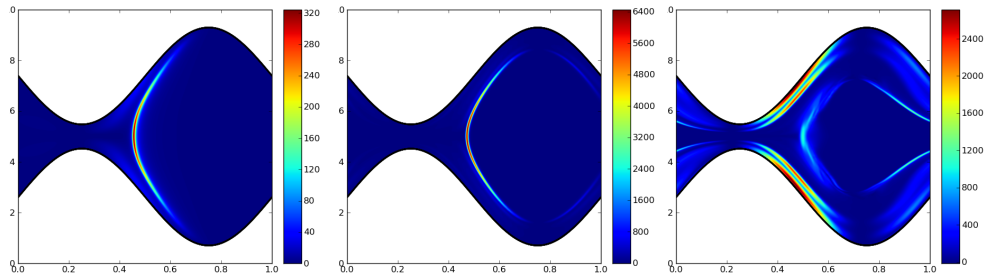


Figure 5: S_{yy} for $We = 5$ and $\chi = 0.8$ at times $t = 0.5, t = 1.5, t = 4.5$.

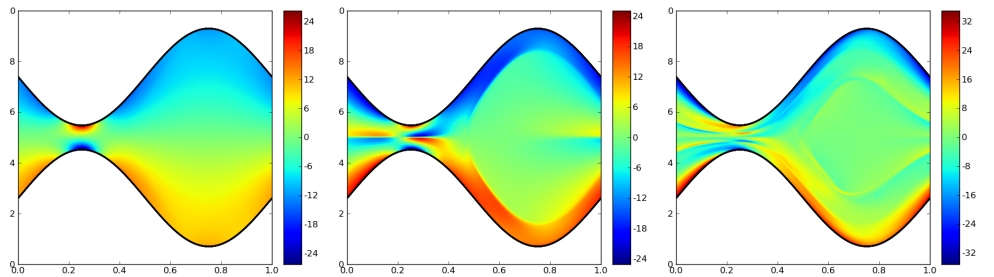


Figure 6: Vorticity for $We = 5$ and $\chi = 0.8$ at times $t = 0.5, t = 1.5, t = 4.5$.

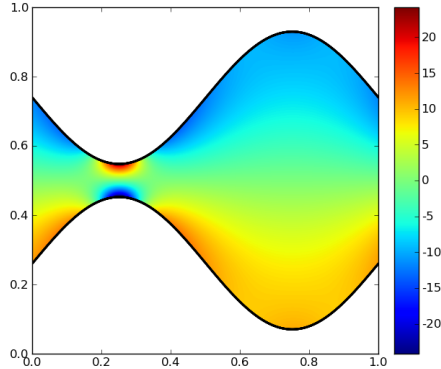


Figure 7: Vorticity for a pump with $\chi = 0.8$ in a Newtonian flow at time $t = 1.5$.

of the walls. We compare the vorticity fields for two numerical resolutions ($N = 512$ and $N = 1024$ with a corresponding $\Delta t = 0.128/N$) and note that the structure is qualitatively identical. Closer examination of the $N = 512$ plot reveals slightly less sharp interfaces, indicative of the greater numerical dissipation (due to the ENO differentiation) at lower resolutions. We observe similar results when we investigate the stress \mathbf{S} .

It is remarkable that the observed layers of high stress effectively block off the interior of the peristaltic pump where the vorticity is nearly zero. Indeed, as Fig. 9 shows, the velocity field at the inner core of the pump is nearly uniform and in the horizontal direction. Consequently, the viscoelastic stresses have isolated a *bolus* of fluid that travels with the peristaltic wave. As time progresses, up to $t = 4.5$, we see the formation of more filamented stress structures closer to the walls as well as two threads of very high stress in the interior of the pump, at the dilated section. The latter two delimit a smaller inner core of nearly uniform flow.

An important observation is that the strong thin filament in S_{xx} at the pump's constriction, around $t = 1.5$, dissipates over time and is significantly weaker at $t = 4.5$. To investigate if this dissipation is inherent to the ENO advection scheme, we perform a resolution study focusing on $\|S_{xx}\|_\infty$ over the time interval $(0, 1.5)$. More precisely, we look at the maximum norm of S_{xx} along the horizontal line of symmetry, denoted as $\|\bar{S}_{xx}(t)\|_\infty$ at time t . First, in Fig. 10(a), we plot $\|\bar{S}_{xx}(t)\|_\infty$ over time for values of N ranging

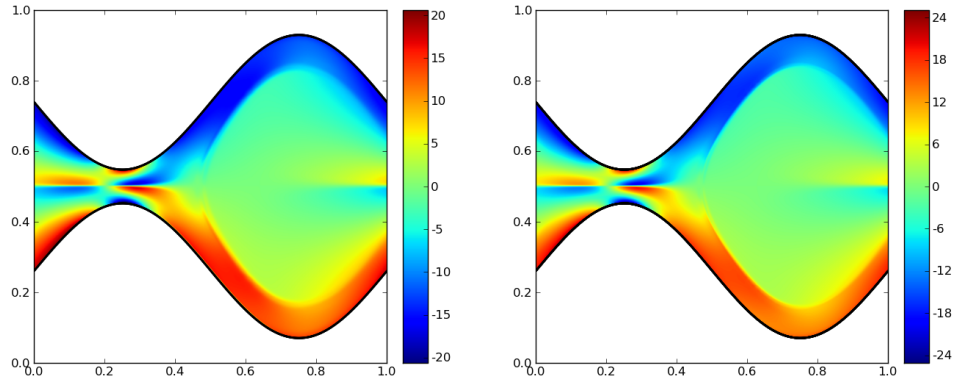


Figure 8: A comparison of the vorticity for $\chi = 0.8$ and $We = 5$ at time $t = 1.5$ for $N = 512$ and $N = 1024$ on the left and right, respectively.

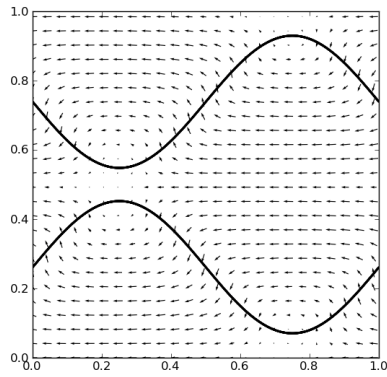


Figure 9: Velocity field for $\chi = 0.8$ and $We = 5$ at time $t = 1.5$.

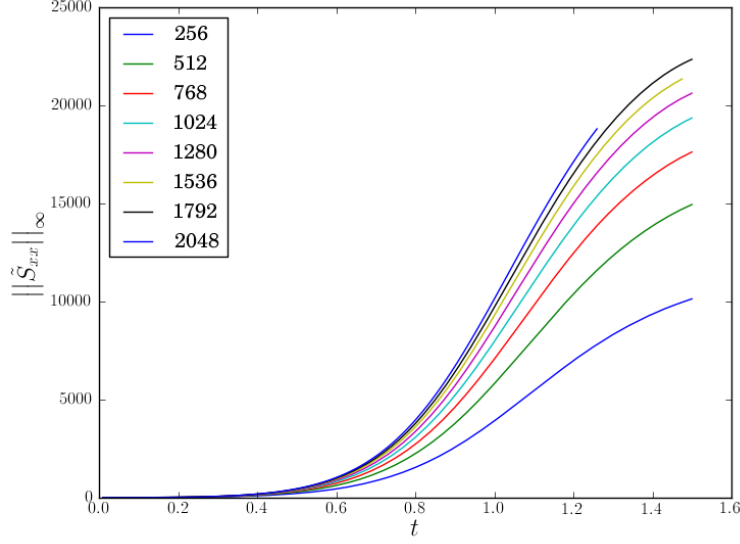
from $N = 256$ to $N = 2048$ ($\Delta t = 0.128/N$). We see that there is a fast, nearly exponential growth of this quantity, that levels off near $t = 1.5$. As N increases, so does the maximum stress. We analyze this dependence in Fig. 10(b) where we plot $\|\bar{S}_{xx}(t)\|_\infty$ at $t = 1.25$ versus $\log N$. We observe that $\|\bar{S}_{xx}(1.25)\|_\infty$ grows almost exactly proportional to $\log N$, yielding the approximate formula

$$\|\bar{S}_{xx}(1.25)\|_\infty \approx 5286 \log N. \quad (23)$$

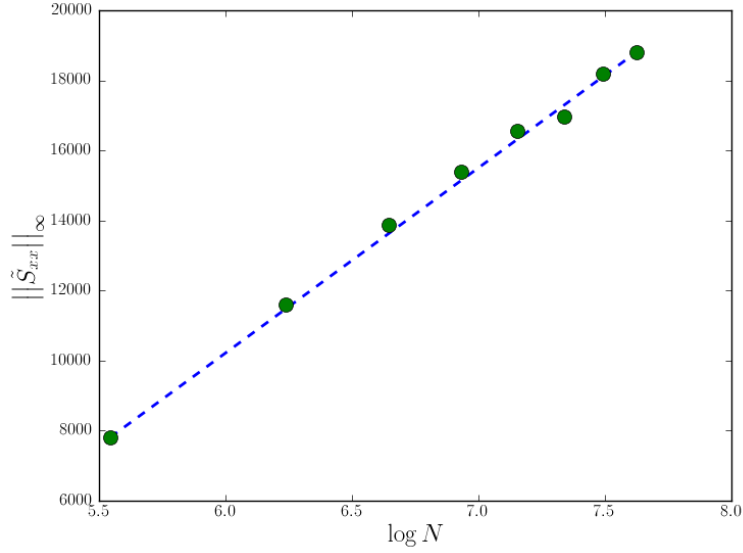
It is unclear if the relationship (23) persists for arbitrarily large N but if this were the case, then it would be evidence for a finite time blow-up singularity in the OB model which is being regularized numerically by the high order ENO upwinding. To provide additional verification, we attempt to fit an exponential time growth model of the form $C_N e^{\beta_N t}$ to $\|\bar{S}_{xx}(t)\|_\infty$ over the time interval $(0.36, 0.70)$. For $N = 2048$, the best fit is given by $C = 10, \beta = 7.68$. The fit is qualitatively good, as seen in Fig. 11(a). We proceed to compute the best fit for various values of N and investigate the sequence $\{\beta_N\}$. In Fig. 11(b), we plot β_N with respect to $\log N$ and notice a distinct linear trend. A linear fit yields $\beta_N \approx 0.3533 \log N$. We thus again see an unbounded growth as $N \rightarrow \infty$. This uncontrolled behavior for the exponent clearly points in the direction of a potential finite-time singularity in the polymeric stress.

Numerical evidence for such a finite time blow-up in an OB fluid has been provided by Thomases and Shelley using a four-roll mill type of background forcing [35]. Much earlier, Rallison and Hinch [26] elucidated this unphysical behavior of the OB model due to the infinite extensibility of the macromolecule coils. It is interesting to note, however, that the seemingly unbounded stress growth occurs in a highly concentrated region which appears to collapse to a line. Thus, as argued in [26], the gigantic but highly localized stresses are unable to arrest the extensional flow causing the unbounded coil elongation.

It is important to emphasize the specific regularizing role of the ENO differentiation in the OB model. If simple, first order upwinding were employed to discretize the advection terms in the polymeric stress equation [Eq. (6)] it would be equivalent to using centered differences with the addition of the diffusion term $\frac{h}{2} L_h \mathbf{S} \approx \frac{h}{2} \nabla^2 \mathbf{S}$, where L_h is the standard second order approximation of the Laplacian. As pointed out recently by Thomases [33], the addition of $O(h) \nabla^2 \mathbf{S}$ diffusion seems to be sufficient to maintain a finite

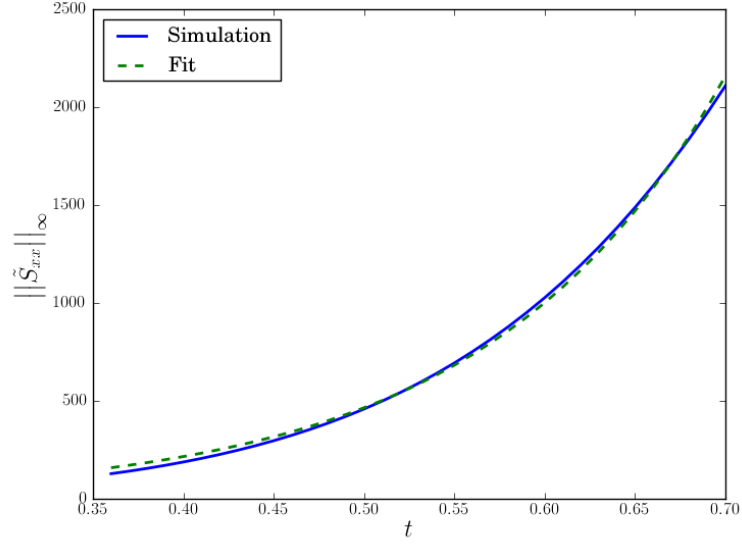


(a) $\|\tilde{S}_{xx}(t)\|_{\infty}$ over the time interval $(0, 1.5)$ for various values of N .

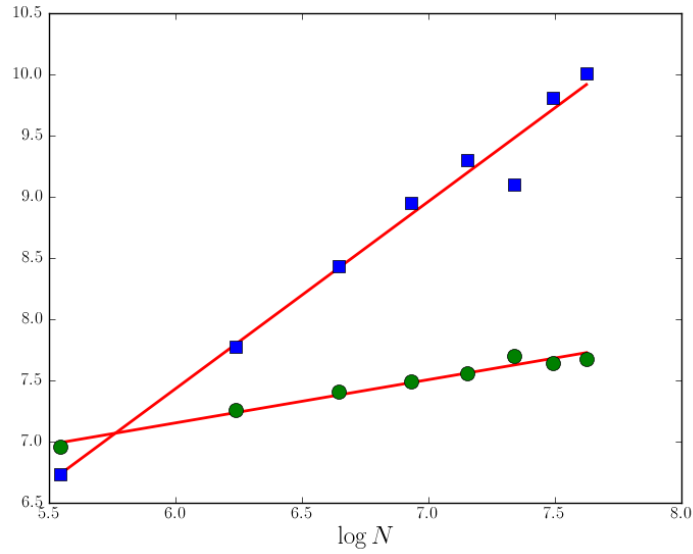


(b) $\|\tilde{S}_{xx}(t)\|_{\infty}$ at time $t = 1.25$, plotted against $\log N$, as N varies from 256 to 2048. Dashed line is a linear fit with slope $m = 5286$

Figure 10: Resolution study of the sup norm of the stress component S_{xx} along the horizontal line of symmetry, denoted as $\|\tilde{S}_{xx}(t)\|_{\infty}$ at time t .



(a) $\|\bar{S}_{xx}(t)\|_\infty$ over the time interval $(0.36, 0.70)$ for $N = 2048$. Matched fit is the exponential curve $10e^{7.68t}$.



(b) β_N (\circ) and C_N (\square) with respect to $\log N$. The solid line is a linear fit with slope $m = 0.3533$.

Figure 11: Time behavior of $\|\bar{S}_{xx}(t)\|_\infty$ for $\chi = 0.8$ and $We = 5$.

polymer coil extension and stress. However, the diffusion provided by the term $\frac{h}{2}L_h\mathbf{S}$ could be excessive for practical resolutions. The ENO scheme, which uses upwinding plus a high order correction employing a sliding stencil, provides a much smaller and localized regularization. In particular, we capture much sharper interfaces in the stress when using ENO as opposed to upwinding.

4.3. High Weissenberg number

As the Weissenberg number increases, the viscoelastic effects on the flow become more pronounced. Large stresses and normal forces on the walls of the peristaltic pump are generated, even for moderate values of We . These forces in turn require large stiffness constants σ to properly maintain the prescribed shape and motion of the walls in the IB model. Previous investigations employing the same model [32, 10] have been limited to $We \leq 5$. Here, we are able to investigate for much higher Weissenberg numbers, in excess to 100.

We begin by considering the case $We = 55$ and $\chi = 0.5$. In Figs. 12 through 15, we plot the polymeric stress and the vorticity evolution over time, for $N = 1024$ and $\Delta t = 0.00025$. Unlike the $We = 5$ and $\chi = 0.8$ case, the stress components S_{xx} and S_{xy} at early times ($t = 1.4$) display doubly-peaked concentrated structures. There is also a new region of strong polymer elongation (as measured by $\text{tr}(\mathbf{S})$) near the center of the dilated part of the pump (see Fig. 14). By $t = 8.4$, the polymeric stress components have evolved into multi-layered structures conforming to the shape of the pump's walls. The vortex pair at the pump's constriction (Fig. 15) has also been deformed by the strong stresses in that area. As time progresses, however, the multi-layered structures merge into smooth, simple regions as observed at $t = 18.9$. It is conceivable that this smoothing transition is due to an accumulation of the numerical dissipation inherent to the ENO advection scheme.

4.4. Mean flow rate behavior

An important question is how the normalized mean flow rate Θ responds to changes in χ and We . In Fig. 16, we plot Θ at time $t = 15$ and $t = 50$ for different values of χ and We in the ranges $0 \leq \chi \leq 0.75$ and $0 \leq We \leq 105$.

At $t = 15$ [Fig. 16(a)], we observe a simple monotonic growth of Θ as χ increases for $We = 1$ and $We = 2$. For the larger We , there is a somewhat oscillatory change at high occlusion ratios, in the range $0.6 \leq \chi \leq 0.75$. We

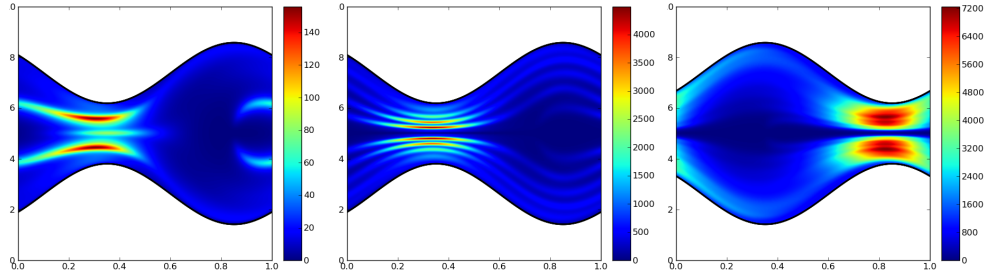


Figure 12: S_{xx} for $We = 55$ and $\chi = 0.5$ at times $t = 1.4$, $t = 8.4$, $t = 18.9$.

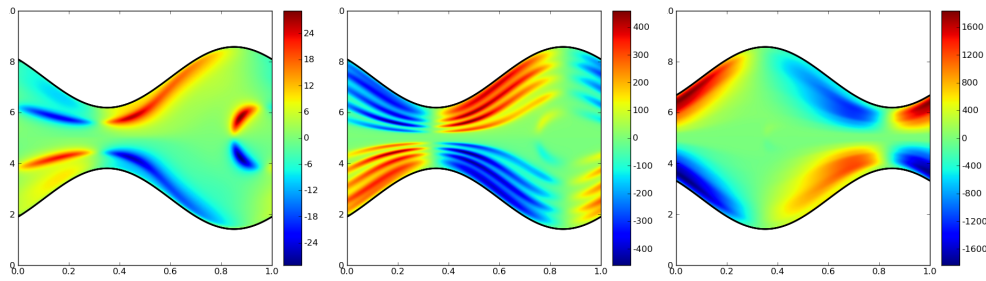


Figure 13: S_{xy} for $We = 55$ and $\chi = 0.5$ at times $t = 1.4$, $t = 8.4$, $t = 18.9$.

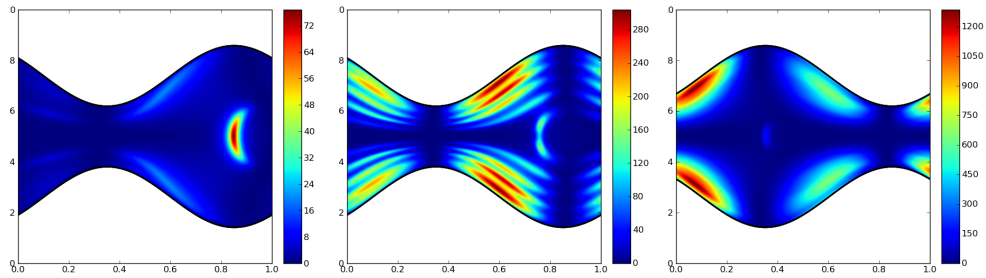


Figure 14: S_{yy} for $We = 55$ and $\chi = 0.5$ at times $t = 1.4$, $t = 8.4$, $t = 18.9$.

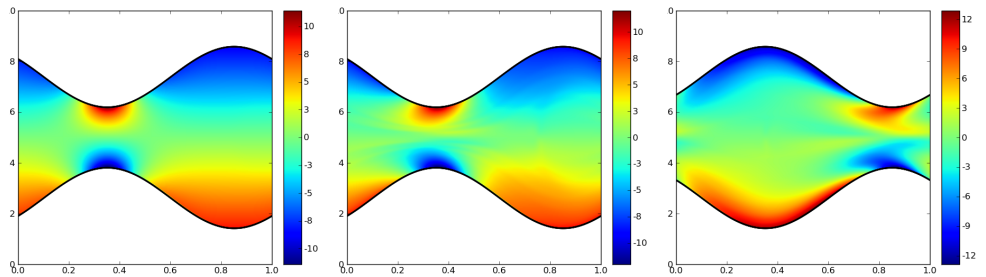


Figure 15: Vorticity for $We = 55$ and $\chi = 0.5$ at times $t = 1.4$, $t = 8.4$, $t = 18.9$.

note that our observed monotonic behavior of Θ for $0 \leq \chi \leq 0.5$ and for all the considered Weissenberg numbers is in contrast to the marked flow decrease near $\chi = 0.5$ reported in [32] for $We = 2$ and $We = 5$. However, in [10] a simple monotonic behavior for $We = 2$ was also observed and only a mild decrease in Θ for $We = 5$ as χ approached 0.5. As pointed out above, we have found that this flow decrease is largely due to an artificial swelling of the pump when the stiffness constant σ in the IB model is not sufficiently large to withstand the enormous stresses generated by the flow for increased values of χ and We .

The simple monotonic growth of Θ for $We = 1$ and $We = 2$ is maintained at $t = 50$ [Fig. 16(b)] for all the examined occlusion ratios, $0 \leq \chi \leq 0.75$. However, the χ -dependence of Θ is qualitatively very different for higher We and for $0.5 \leq \chi \leq 0.75$. First, there is a critical occlusion ratio $\chi_c \approx 0.475$ after which the monotonic increase of Θ with We is essentially reversed (with the exception of $We = 105$ for the largest two occlusion ratios). Moreover, the mean flow rate appears to converge in We to a nearly flat curve for $\chi_c \leq \chi < 0.7$ before increasing toward the expected value of 1 as $\chi \rightarrow 1$. Indeed, there is little difference between the $We = 55$ and the $We = 105$ curves. This could be indicative of a dominant effect of numerical regularization (via the ENO scheme) as computations for $We = 105$ for higher resolutions become unstable.

To try to understand the pronounced deviation from the Newtonian case, we look at the time dependence of Θ . For $We \leq 5$, it appears that a quasi-steady state is eventually reached and, as reported in [32, 10], it takes a time of about $3We$ to attain that regime. For higher We , we find that the situation is substantially different and quite more complex. Figure 17 displays the time behavior of Θ for $\chi = 0.4$ and $\chi = 0.6$. At the smaller occlusion ratio [Fig. 17(a)], the mean flow for $We = 5$ has little variation over time, consistent with previous results. However, for $We \geq 25$ both small amplitude oscillations at the order of the pump's period as well as sizable longer time scale variations are observed. In particular, there is no apparent quasi-steady state for $We = 55$ and $We = 105$ up to $t \leq 150$. Nevertheless, for $We = 25$ there is a near plateau from approximately $t = 70$ to $t = 120$ and after which Θ undergoes a noticeable decrease. This type of transition also occurs for $We = 5$ at the higher occlusion ratio $\chi = 0.6$ [Fig. 17(b)]. The flow appears to reach and maintain a quasi-steady value of Θ for about 50 periods (from $t = 20$ to $t = 70$) but then has a sudden drop at time $t = 70$. This surprising mean flow rate transition takes place soon

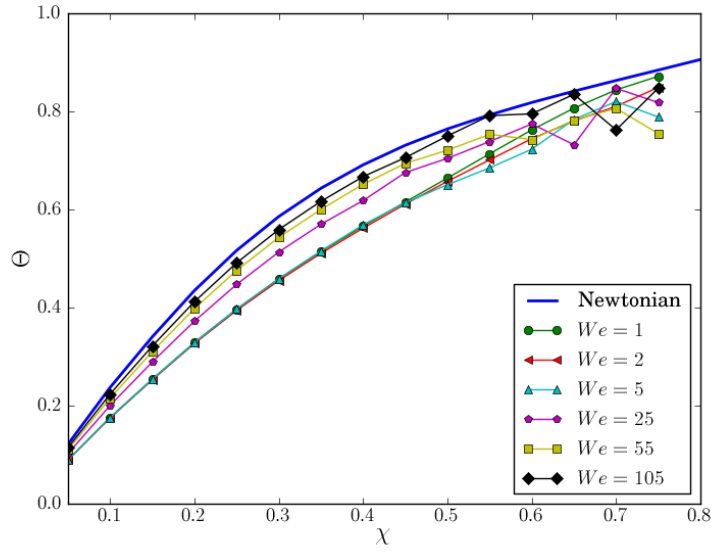
after we begin to observe a loss of symmetry in the flow. Figure 18 shows the extent to which the vorticity field has become asymmetric for $We = 5$ and $\chi = 6$ at $t = 150$. We believe that this *symmetry breaking transition* is due to elastic flow instabilities excited by asymmetric perturbations of the flow variables (introduced, for example, by the matrix approximation of the flow-structure interaction operator). Asymmetric flow transitions have been observed experimentally in a dilute solution of flexible polymers [1] as well as in numerical simulations of the OB model [23, 37, 3, 34]. They are associated with strong extensional flows that produce large polymer coil elongations which is precisely the case for the peristaltic pump at sufficiently high Weissenberg numbers and large occlusion ratios.

5. Conclusions

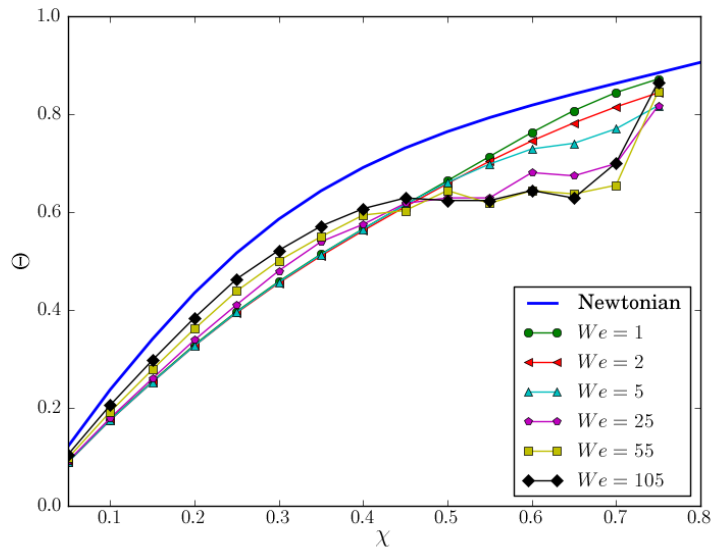
We presented a numerical investigation of peristaltic pumping of a viscoelastic fluid using the simple OB model coupled to the Navier-Stokes equations. Using a fast and non-stiff IB method we were able to explore, for the first time, parameter regimes that include nearly the entire range of occlusion ratios and Weissenberg numbers in excess of 100. Rich, time-dependent stress structures and striking new flow behaviors emerged. The investigation also pointed to the limitations of the OB model (potential finite time blow-up) and to the role numerical regularization plays.

Our study reveals that for large occlusion ratios and moderate to large Weissenberg numbers (e.g. $\chi = 0.8$ and $We = 5$), the polymeric stress develops highly concentrated, filamented structures. At the pump's constriction, an unbounded polymer coil elongation along the line of symmetry can occur due to a strong extensional flow. This eventually leads to a finite time singularity in the the solution as the mesh size goes to zero. However, at a finite resolution the high order ENO upwinding employed in the polymeric stress equation is sufficient to obtain a smooth solution for long times. In this long-time solution, we observe vorticity layers around the inner part of the pump's walls which at some time effectively isolate a *bolus* of fluid that travels with the peristaltic wave.

As the Weissenberg number increases our numerical simulations show that the flow becomes highly time-dependent with complex dynamics. This is reflected in the behavior of the mean flow rate Θ . After 15 time periods, we see a nearly monotonic growth of Θ with χ for $We \leq 5$ and $0 \leq \chi \leq 0.75$ and an increase in Θ with We for fixed χ . Several periods later, there is

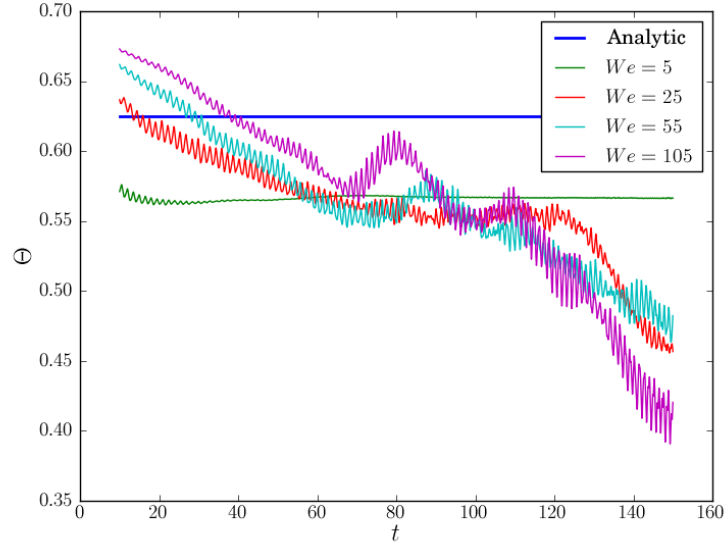


(a) Normalized mean flow rate versus χ at $t = 15$.

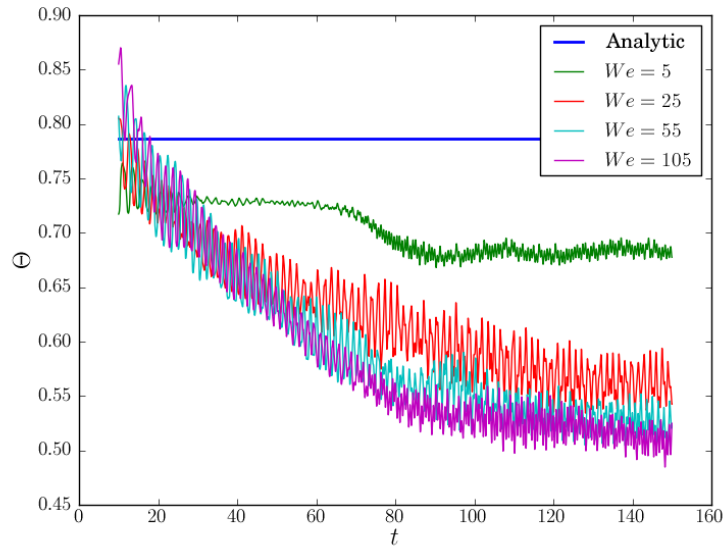


(b) Normalized mean flow rate versus χ at $t = 50$.

Figure 16: Normalized mean flow rate for various values of We and χ .



(a) $\chi = 0.4$



(b) $\chi = 0.6$

Figure 17: Mean flow Θ over time for various values of We . Top and bottom plot are for $\chi = 0.4$ and $\chi = 0.6$ respectively.

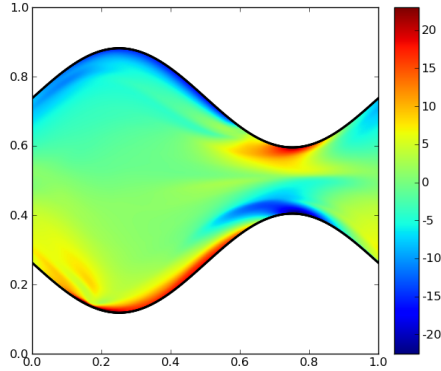


Figure 18: Velocity field for $\chi = 0.8$ and $We = 5$ at time $t = 1.5$.

an emergence of a critical χ_c at which the ordering in We is reversed (flow decreases with increasing We) and the mean flow rate appears to converge in We to a nearly flat curve for $\chi_c \leq \chi < 0.7$. Moreover, for moderate We , we are able to observe a symmetry breaking transition after which there is a decrease in Θ and the flow migrates from one quasi-steady state to another.

Future work will focus on the three-dimensional flow where preliminary results suggest new behaviors. In 3D, it is also possible to study a plethora of novel asymmetrical pump geometries, including cork-screw like shapes. Preliminary results also suggest interesting differences when the OB fluid is replaced with a FENE-P fluid to maintain finite coil extensibility.

Acknowledgments

The authors would like to thank John Crispell for sharing detailed aspects of his experience simulating the OB model for peristaltic pumping. Computations were performed on the Knot Cluster at the California NanoSystems Institute (CNSI) Computing Facility, funded by the National Science Foundation under grant CNS-0960316. Special thanks to Fuzzy Rogers and Paul Weakliem at CNSI for their help working with the cluster. The authors gratefully acknowledge partial support for this work by the National Science Foundation under grant DMS-1016310.

References

- [1] P. E. Arratia, C. C. Thomas, J. Diorio, and J. P. Gollub. Elastic instabilities of polymer solutions in cross-channel flow. *Physical Review Letters*, 96:144502, 2006.
- [2] E. Bardan, P. Y. Xie, J. L. Ren, K. W. Dua, and R. Shaker. Effect of pharyngeal water stimulation on esophageal peristalsis and bolus transport. *American Journal of Physiology-Gastrointestinal and Liver Physiology*, 272(2):G265–G271, 1997.
- [3] S. Berti, A. Bistagnino, G. Boffetta, A. Celani, and S. Musacchio. Two-dimensional elastic turbulence. *Physical Review E*, 77:055306(R), 2008.
- [4] R. B. Bird, C. F. Curtiss, R. C. Armstrong, and O. Hassager. *Dynamics of Polymeric Liquids. Volume 2: Kinetic Theory*. John Wiley and Sons, New York, 1987.
- [5] J.R. Blake, P.G. Vann, and H. Winet. A model of ovum transport. *Journal of Theoretical Biology*, 102(1):145–166, 1983.
- [6] G. Bohme and R. Friedrich. Peristaltic flow of viscoelastic liquids. *Journal of Fluid Mechanics*, 128:109–122, 1983.
- [7] H. D. Ceniceros and J. E. Fisher. A fast, robust, and non-stiff immersed boundary method. *Journal of Computational Physics*, 230(12):5133–5153, 2011.
- [8] H. D. Ceniceros, J. E. Fisher, and A. M. Roma. Efficient solutions to robust, semi-implicit discretizations of the immersed boundary method. *Journal of Computational Physics*, 228(19):7137–7158, 2009.
- [9] J. Chripell. Private communication.
- [10] J. Chripell and L. Fauci. Peristaltic pumping of solid particles immersed in a viscoelastic fluid. *Math. Model. Nat. Phenom.*, 6(5):67–83, 2011.
- [11] K. Connington, Q. Kang, H. Viswanathan, A. Abdel-Fattah, and S. Chen. Peristaltic particle transport using the lattice Boltzmann method. *Physics of Fluids*, 21(5):053301, May 2009.

- [12] M. Doi and S. F. Edwards. *The Theory of Polymer Dynamics*. Oxford University Press, 1986.
- [13] L. J. Fauci. Peristaltic pumping of solid particles. *Computers & Fluids*, 21(4):583–598, 1992.
- [14] T. Ishikawa, T. Sato, G. Mohit, Y. Imai, and T. Yamaguchi. Transport phenomena of microbial flora in the small intestine with peristalsis. *Journal of Theoretical Biology*, 279(1):63–73, 2011.
- [15] M. Y. Jaffrin. Inertia and streamline curvature effects on peristaltic pumping. *Int. J. Engng. Sci.*, 11:681–699, 1973.
- [16] M. Y. Jaffrin and A. H. Shapiro. Peristaltic pumping. *Annual Review of Fluid Mechanics*, 3(1):13–37, 1971.
- [17] R. P. Jansen and V. K. Bajpai. Oviduct acid mucus glycoproteins in the estrous rabbit - ultrastructure and histochemistry. *Biology of Reproduction*, 26(1):155–168, 1982.
- [18] G. Kunz, D. Beil, H. Deiniger, A. Einspanier, G. Mall, and G. Leyendecker. The uterine peristaltic pump. normal and impeded sperm transport within the female genital tract. *Adv. Exp. Med. Biol.*, 424:267–277, 1997.
- [19] R. G. Larson. *The Structure and Rheology of Complex Fluids*. Oxford University Press, Oxford, 1999.
- [20] Y. Mori. Convergence proof of the velocity field for a Stokes flow immersed boundary method. *Communications on Pure and Applied Mathematics*, 61:1213–1263, 2008.
- [21] C. S. Peskin. Numerical analysis of blood flow in the heart. *J. Comput. Phys*, 25:220–252, 1977.
- [22] C. S. Peskin. The immersed boundary method. *Acta Numerica*, pages 477–517, 2002.
- [23] R. J. Poole, M. A. Alves, and P. J. Oliveira. Purely elastic flow asymmetries. *Physical Review Letters*, 99:164503, 2007.

- [24] C. Pozrikidis. A study of peristaltic flow. *Journal of Fluid Mechanics*, 180:515–527, 1987.
- [25] K. J. Quillin. Kinematic scaling of locomotion by hydrostatic animals: Ontogeny of peristaltic crawling by the earthworm *Lumbricus terrestris*. *J. Exp. Biol.*, 424:267, 1997.
- [26] J. M. Rallison and E. J. Hinch. Do we understand the physics in the constitutive equation? *Journal of Non-Newtonian Fluid Mechanics*, 29:37–55, 1988.
- [27] A. H. Shapiro, M. Y. Jaffrin, and S. L. Weinberg. Peristaltic pumping with long wavelengths at low Reynolds number. *J. Fluid Mech.*, 37:799–825, 1969.
- [28] C. W. Shu and S. Osher. Efficient implementation of essentially non-oscillatory shock capturing schemes. *J. Comput. Phys.*, 88:439, 1988.
- [29] L. M. Srivastava and V. P. Srivastava. Peristaltic Transport of a Particle-Fluid Suspension. *Journal of Biomechanical Engineering-Transactions Oof The ASME*, 111(2):157–165, May 1989.
- [30] J. M. Stockie and B. R. Wetton. Analysis of stiffness in the immersed boundary method and implications for time-stepping schemes. *J. Comput. Phys.*, 154:41–64, 1999.
- [31] J. M. Stockie and B. T. R. Wetton. Stability analysis for the immersed fiber problem. *SIAM J. Appl. Math.*, 55(6):1577–1591, 1995.
- [32] J. Teran, L. Fauci, and M. Shelley. Peristaltic pumping and irreversibility of a stokesian viscoelastic fluid. *Physics of Fluids*, 20:073101, 2008.
- [33] B. Thomases. An analysis of stress diffusion on the dynamics of creeping viscoelastic flow. *Journal of Non-Newtonian Fluid Mechanics*, 166:1221–1228, 2011.
- [34] B. Thomases and M. Shelley. Transition to mixing and oscillations in a Stokesian viscoelastic flow. *Physical Review Letters*, 103:094501, 2009.
- [35] B. Thomases and M. J. Shelley. Emergence of singular structures in Oldroyd B fluids. *Physics of fluids*, 19:103103, 2007.

- [36] D. Tripathi. Peristaltic transport of a viscoelastic fluid in a channel. *Acta Astronautica*, 68(7-8):1379–1385, Apr-May 2011.
- [37] L. Xi and M. D. Graham. A mechanism for oscillatory instability in viscoelastic cross-slot flow. *J. Fluid Mech.*, 622:145–165, 209.